J Mater Sci (2010) 45:946–952
DOI 10.1007/s10853-009-4024-4

Structure and electrochemical hydrogen storage properties of Pd/$Mg_{1-x}Al_x$/Pd thin films prepared by pulsed laser deposition

S. Bouhtiyya · L. Roué

Received: 2 October 2009 / Accepted: 6 November 2009 / Published online: 19 November 2009

Abstract Three-layered Pd/$Mg_{1-x}Al_x$/Pd ($x = 0$, 0.13, 0.21, 0.39) thin films were prepared by means of pulsed laser deposition. In the present Al concentration range, X-ray diffraction analyses showed that the $Mg_{1-x}Al_x$ layer was constituted of a single phase Mg(Al) solid solution. The Mg(Al) grains are preferentially orientated along the *c*-axis and their size decreased (from 18.5 to 10.5 nm) as the Al content increased. Scanning electron microscopy and atomic force microscopy observations indicated that all the films exhibited a globular surface structure. However, the surface roughness of the films decreased as the Al concentration increased. Rutherford backscattering spectroscopy revealed that the Mg–Al layer density (porosity) was strongly dependent on the Al content. Successive hydriding charge/discharge cycles were performed on the different Pd/$Mg_{1-x}Al_x$/Pd films in alkaline media. The highest discharge capacity was obtained with the Pd/$Mg_{0.79}Al_{0.21}$/Pd film, namely ~85 μAh cm^{-2} μm^{-1} or 320 mAh g^{-1}, which corresponds to a H/M atomic ratio of ~0.48 in the Mg–Al layer.

Introduction

As H_2 sources for fuel cells, metal hydrides are a good alternative to conventional high-pressure hydrogen storage vessels thanks to their high hydrogen storage capacities and safety aspects [1]. Moreover, metal hydrides are potential candidates for other applications as well [2], including gas purifiers, isotope separators, hydrogen sensors, thermal compressors, optical windows, Ni-MH batteries and more recently Li-ion batteries [3].

Magnesium is one of the best materials for hydrogen storage due to its high H-storage capacity (7.6 wt% for MgH_2) and low cost. However, it suffers from several drawbacks: (i) the high thermodynamic stability of MgH_2 ($\Delta H_f \sim -75$ kJ mol^{-1}) necessitates high temperatures (~300 °C) for hydrogen desorption at 1 bar, (ii) the energy barrier for H_2 dissociation on Mg is high ($E_a \sim 72$ kJ mol^{-1} H_2) [4] and hydrogen diffusion in MgH_2 phase is very slow ($D_H \sim 10^{-16}$ cm^2 s^{-1}) [5], leading to slow hydrogen absorption/desorption kinetics, (iii) magnesium is very air sensitive, creating a native oxide surface layer which makes Mg hard to activate.

A number of strategies have been explored to improve the hydrogenation thermodynamics and kinetics of Mg [6]: reducing the Mg grain size to the nanometer scale, adding hydrogenation catalysts (Pd, V, Cr_2O_3, etc.) and alloying Mg with various elements (Ni, Pd, Co, Al, etc.). Most of these Mg-based materials have been produced in powder form by high energy ball milling [7]. However, thin film processing is an alternate method that offers the possibility to synthesise nanostructured Mg-based materials in well-defined compositions, microstructures and dimensions. Moreover, kinetic limitations can be minimised and cooperative phenomena can be induced through the synthesis of multilayered films, leading to novel materials with unique hydrogen storage properties [8–13].

We have recently shown that pulsed laser deposition (PLD) is a suitable technique to prepare nanostructured Pd/Mg/Pd thin films with variable microstructures depending on the deposition parameters [13]. It was demonstrated that the increase in pressure of the background helium gas in the PLD chamber for Mg deposition increased the roughness of the Mg layer, leading to an unsharp Pd_{out}/Mg

S. Bouhtiyya · L. Roué (✉)
INRS-Énergie, Matériaux et Télécommunications, 1650 Boulevard Lionel Boulet, Varennes, QC J3X 1S2, Canada
e-mail: roue@emt.inrs.ca

interface region. This has a positive influence on the electrochemical hydriding properties of the films. However, the maximum H-solubility in the Mg layer (170 nm in thickness) remains low (H/Mg $\sim$0.26) because the formation of MgH_2 is confined to the Pd_{out}/Mg interface region and thus, a large part of the Mg layer does not participate in the electrochemical hydriding process.

Here, we report the structure and electrochemical hydriding behaviour of three-layered Pd/$Mg_{1-x}Al_x$/Pd thin films synthesised by means of pulsed laser deposition using optimum He pressure in the PLD chamber as determined previously from Pd/Mg/Pd films [13]. The addition of Al to Mg was inspired by several studies (see Andreasen's recent review on the hydrogenation properties of Mg–Al alloys [14]) which showed that the thermodynamics and kinetics of hydrogenation/dehydrogenation of Mg–Al alloys are generally improved compared to Mg alone.

Experimental

Film preparation

Three-layered Pd/$Mg_{1-x}Al_x$/Pd ($x = 0$, 0.13, 0.21, 0.39) thin films were prepared by means of pulsed laser deposition at room temperature using a pulsed KrF excimer laser ($\lambda = 248$ nm, pulse width = 20 ns, repetition rate = 50 Hz). The deposition times were controlled in order to achieve Pd and Mg–Al layer thicknesses of ca. 15 and 200 nm, respectively, for all films. The Mg–Al layer with controlled Al content was deposited using composite Mg–Al targets consisting on separate zones of magnesium (99.95%; Alfa Æsar) and aluminium (99.9%; Alfa Æsar) foils, in which the surface area of each element was determined on the basis of their deposition rate calculated after a preliminary set of ablation tests on the separate metals. The alternate targets for ablation were a composite Mg–Al target and a palladium foil (99.9%; Alfa Æsar). Prior to deposition, the chamber was evacuated to a pressure of ca. 10^{-4} Pa. Depositions were made in the presence of helium (4.8 grade) at a partial pressure of 200 mTorr ($\sim$27 Pa) for the Pd layers and a partial pressure of 600 mTorr ($\sim$80 Pa) for the Mg–Al layer. The laser beam was focused at a 45° angle on the target with a spot area of 1.7 mm^2. The targets were moved continuously via a dual rotation and translation motion during ablation to ensure uniform ablation of the target. During the deposition, the laser fluence was kept at 5.0 $\pm$ 0.1 J/cm^2 (250 MW/cm^2). The substrate holder was spun around its normal axis during deposition. The target and the substrate holder were parallel and the distance between them was set to 4 cm. Films were deposited on mirror-polished nickel disks (geometric surface area = 1 cm^2). Eight substrates were placed symmetrically around the centre of the substrate holder at a radial distance of 2 cm.

Film characterisation

The total thickness of the films was determined by using a Dektak profilometer and the thickness of each layer was measured from scanning electron microscopy (SEM) observations in cross-section.

Atomic force microscopy (AFM) investigations were performed under ambient conditions with a Nanoscope III microscope from Digital Instruments operated in contact mode using standard Si_3N_4 tips.

Rutherford backscattering spectroscopy (RBS) with 2 MeV $^4He^{++}$ was used to determine the film composition and density. The Mg/Al atomic ratios of the films were also determined by energy dispersive X-ray spectroscopy (EDS) and were consistent with the RBS analyses.

The film structure was analysed by X-ray diffraction (XRD) measurements in Bragg–Brentano θ–2θ configuration using the Cu Kα radiation ($\lambda = 1.5414$ Å).

The electrochemical experiments were carried out using a Voltalab40 (Radiometer Analytical) potentiostat/galvanostat. Tests were performed at room temperature in 1 M KOH solution with a three-electrode cell. The counter-electrode was a Pt wire and the reference electrode was an Hg/HgO electrode (Koslow).

Results and discussion

The main characteristics of the different samples presented below are summarised in Table 1.

Table 1 Main characteristics of the Mg–Al layer in the different Pd/$Mg_{1-x}Al_x$/Pd samples

Al content (at.%)	*c* Lattice constant (Å)	Crystallite size (nm)	Density (g cm^{-3})	Porosity (%)	Max. discharge capacity (μA cm^{-2} μm^{-1})
0	5.189	18.5	1.39	20	55
13	5.166	15.1	2.15	0	36
21	5.154	14.6	1.28	28	85
39	5.143	10.5	1.83	0	48

Film structure

XRD patterns of the Pd/$Mg_{1-x}Al_x$/Pd ($x = 0$, 0.13, 0.21, 0.39) are shown in Fig. 1. Peaks related to hcp Mg and fcc Pd phases are clearly discernable. The XRD patterns show no evidence of the formation of $Mg_{17}Al_{12}$, Mg_2Al_3 or pure Al phase, as confirmed on XRD patterns in the 2θ region extending from 30° to 60° (not shown). The crystal structure of the Pd layer is similar for the different films with a crystallite size of 13 ± 1 nm (calculated from (111) peak broadening using Scherrer's formula), a preferential orientation in the ⟨111⟩ direction and no significant lattice deformation ($a = 3.895$ Å compared to 3.890 Å for standard Pd).

As clearly shown in Fig. 1, the most intense peak of the Mg phase is the (002)-peak for all films. This indicates a preferential orientation of the Mg grains along the *c*-axis, i.e. perpendicular to the substrate surface. This corroborates previous studies on Mg [8, 13] and Mg–Al [15, 16] thin films and it reflects the lowest surface energy plane of the (001)-plane in Mg crystal. On the basis of the Mg (002) peak position, the lattice parameter *c* of Mg in the Pd/Mg/Pd sample ($c = 5.19$ Å) is smaller than that of standard Mg ($c = 5.21$ Å), indicating that the film is strained, as commonly observed on metal films prepared by PLD [17]. Moreover, a shift in the Mg peak position towards larger 2θ angles with increasing Al content is clearly apparent in Fig. 1. The resulting change of the lattice constant *c* of Mg with respect to the Al content is shown in Fig. 2. The

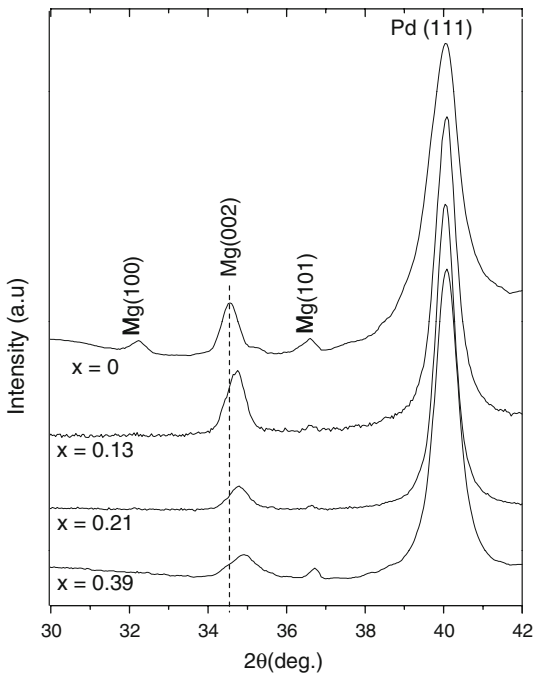

Fig. 1 XRD patterns of the Pd/$Mg_{1-x}Al_x$/Pd films with $x = 0$, 0.13, 0.21 and 0.39

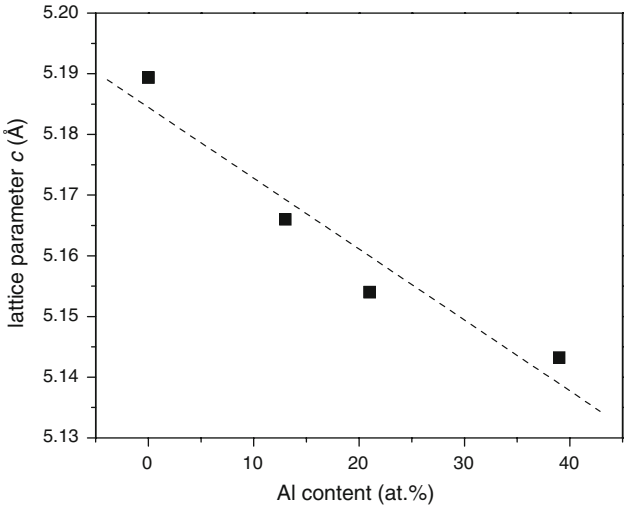

Fig. 2 Evolution of the Mg(Al) lattice parameter *c* (Å) as a function of the Al content in the Mg–Al layer (at.%)

c-lattice value varies approximately linearly from 5.19 to 5.14 Å as the Al content increases from 0 to 39 at.%. This is consistent with the fact that the atomic radius of Al is smaller than that of Mg (1.43 and 1.60 Å, respectively) and it confirms the formation of a Mg(Al) solid solution in the 0–39 at.% aluminium concentration range. This strongly contrasts with the equilibrium limit of solubility of Al in hcp Mg which is <5 at.%, according to the Mg–Al phase diagram [18] and highlights the remarkable ability of the PLD technique to produce supersaturated single phase solid solution of Mg(Al) in a large Al concentration range. A solid solubility extension of Al in Mg was also achieved by magnetron sputtering [19, 20]. Furthermore, as shown in Fig. 3, the Mg(Al) crystallite size (evaluated from (002)

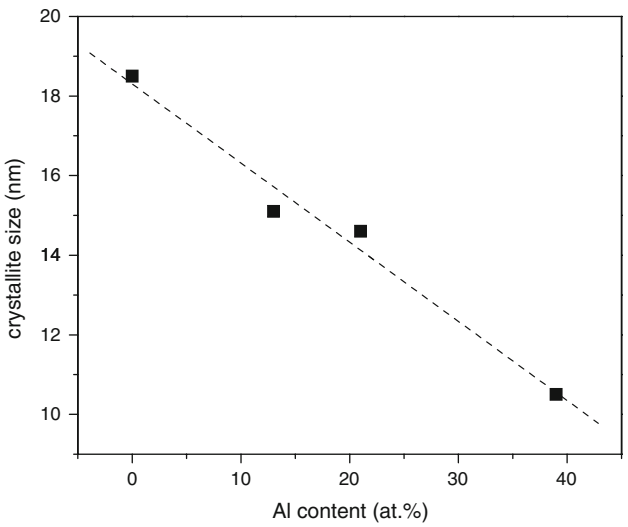

Fig. 3 Evolution of the Mg(Al) crystallite size (nm) as a function of the Al content in the Mg–Al layer (at.%)

peak broadening using Scherrer's formula) decreases approximately linearly from 18.5 to 10.5 nm with the increasing Al content. This crystallinity deterioration of the Mg–Al layer as the Al concentration increases may be due to the segregation of Al atoms in grain boundaries, affecting the grain coalescence.

Film morphology

SEM and AFM observations of the different Pd/$Mg_{1-x}Al_x$/Pd films are shown in Fig. 4. All films exhibit a globular surface structure. However, the surface roughness of the films decreases as the Al concentration increases. In the absence of Al ($x = 0$), the film is very rough (root-mean-square roughness $R_q = 79$ nm) and consists of large particles (mean lateral size $Ø_l$ >100 nm). Moreover, the outermost Pd/Mg interface is not well-defined and irregular whereas a sharp and flat interface is distinguishable between the Mg layer and the Pd underlayer as observed in a previous study [13]. As the Al content increases in the Mg–Al layer, the R_q and $Ø_l$ values decreases, namely $R_q = 44$, 15, 12 nm and $Ø_l \sim 100$, 80 and 60 nm for $x = 0.13$, 0.21 and 0.39, respectively. Few droplets with a diameter in the range of several hundred nanometers (see SEM cross-section images) are formed on the films. Such droplets are often observed on thin films prepared by PLD and are due to the explosive-like character of the target atomization upon PLD [17]. No evident differences in the morphology of the Mg–Al layer between the films are observed from SEM cross-section images. However, on the basis of the RBS measurements, the density of the Mg–Al layer significantly differs from the different samples:

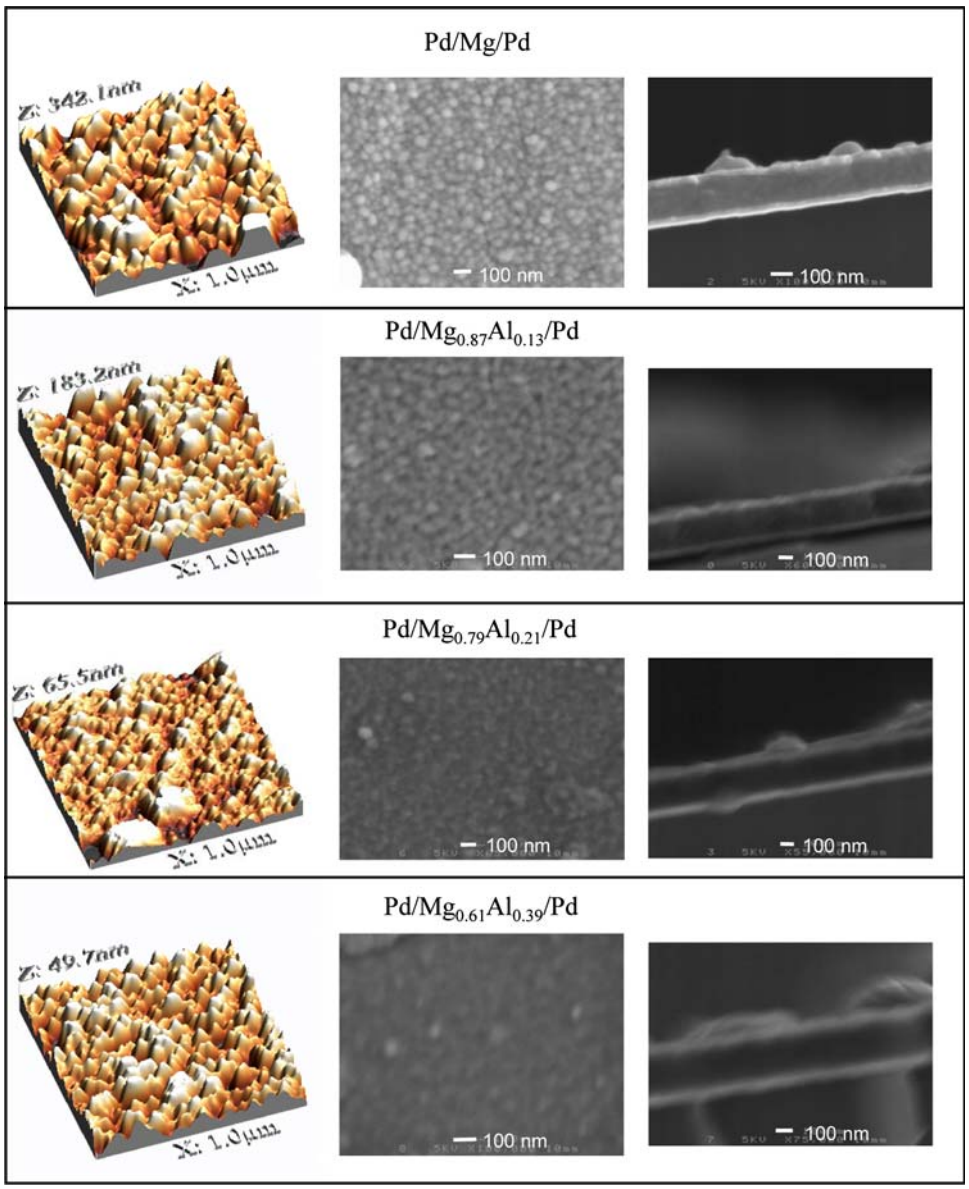

Fig. 4 3D AFM images, surface and cross-section SEM images of the Pd/$Mg_{1-x}Al_x$/Pd films with $x = 0$, 0.13, 0.21 and 0.39

namely, 1.39, 2.15, 1.27 and 1.83 g cm^{-3} for $x = 0$, 0.13, 0.21 and 0.39, respectively. By comparing with the density of the Mg(Al) phases calculated from their unit cell volume determined from XRD analyses, the degree of porosity of the Mg–Al layer is estimated at $\sim$20% for $x = 0$, 28% for $x = 0.21$, whereas no porosity was obtained for $x = 0.13$ and 0.39. The erratic evolution of the Mg–Al layer porosity with its Al content is presently unclear. It may be related to the macroscopic inhomogeneity in the composition of the Mg–Al targets, affecting in an uncontrolled way the distribution of the Mg and Al species in the ablation plume. This may influence the film growing mode and thus, its density. The uncontrolled formation of droplets during film deposition as stated previously may also affect its density. On the other hand, the densities of the inner and outer Pd layers are similar for the different films ($\sim$12 g cm^{-3}) and in accordance with that of bulk Pd (12.02 g cm^{-3}), suggesting the absence of porosity in the Pd layers.

Electrochemical hydriding behaviour

Successive galvanostatic charge/discharge cycles were performed on the different Pd/$Mg_{1-x}Al_x$/Pd films. For the charge, the electrode was fully hydrogenated by applying a current of -500 μA cm^{-2} for 10 min while the discharge was done at 50 μA cm^{-2} with an end-discharge potential fixed at -0.2 V. The experiments were carried out under stirring and Ar bubbling in order to eliminate H_2 molecules accumulated near the electrode (formed during the charge step through the hydrogen evolution reaction) that could be oxidised during the discharge step. Moreover, between each charge/discharge cycle, the electrode was cycled 5 times between -0.45 and 0.45 V at 50 mV s^{-1} for stripping the metallic impurities (coming from the electrolyte) that may be accumulated on the electrode during the charge step, affecting the discharge response as shown previously on Pd thin films [21]. The obtained *E–t* discharge curves at the 1st, 5th and 10th cycles are presented in Fig. 5 for the different Pd/$Mg_{1-x}Al_x$/Pd films. No major evolution in the discharge curves was observed between the 10th and 35th cycles (not shown) and thus, it is assumed that at the 10th cycle, the electrodes have reached their steady state.

For $x = 0$ (Fig. 5a), the discharge curve at the 10th cycle displays a well-defined plateau at about -0.75 V attributed to the H-desorption reaction. Note that no distinctive H-desorption steps related, respectively, to the Pd and Mg layers are clearly discernable. When the hydrogen desorption reaction is completed, a rapid increase of the potential is observed. Between the 1st and the 10th discharge, a progressive increase of the discharge duration from 630 to 920 s is observed in addition to a modification of the *E–t* curve shape resulting in the disappearance of the discontinuities of the discharge curve. It might reflect some microstructural

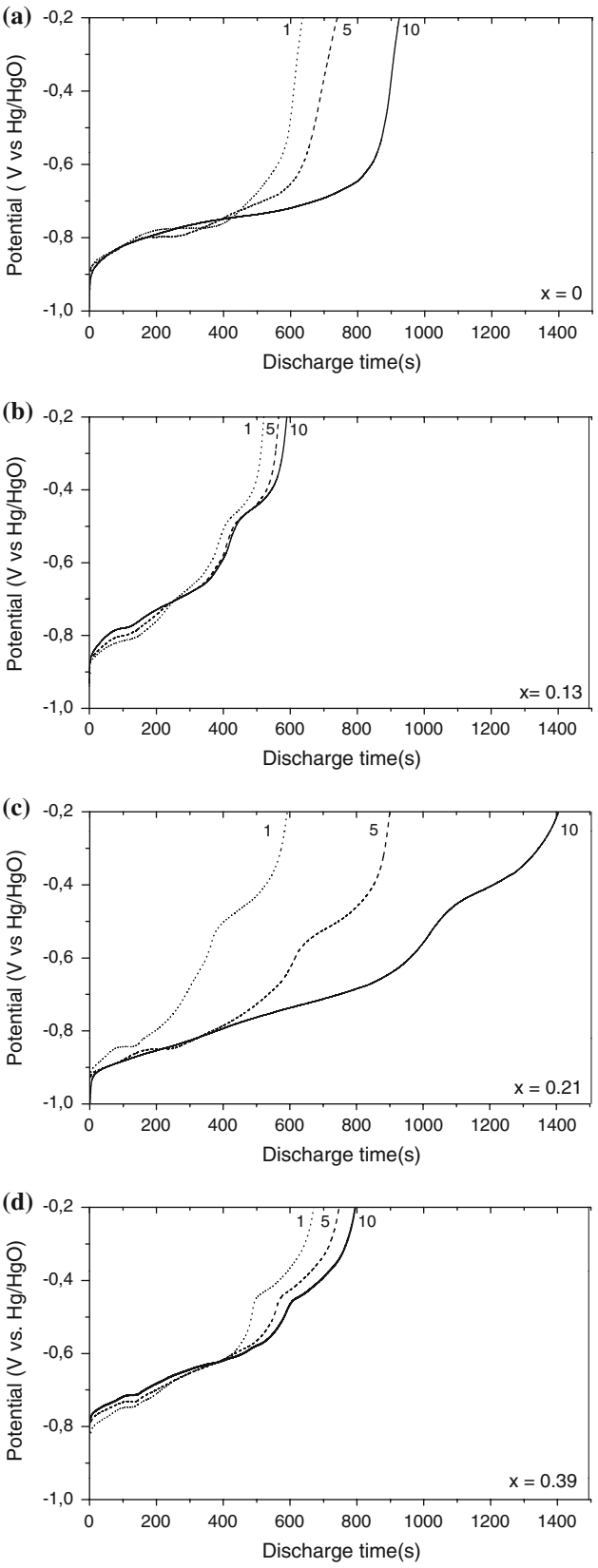

Fig. 5 Discharge curves at the 1st, 5th and 10th cycles of the Pd/$Mg_{1-x}Al_x$/Pd films for **a** $x = 0$, **b** $x = 0.13$, **c** $x = 0.21$ and **d** $x = 0.39$. Discharge current: 50 μA cm^{-2}

reorganization in the film due to its expansion–contraction upon H-absorption/desorption cycling. On the basis of the maximum discharge duration (920 s), the discharge capacity of the Pd/Mg/Pd film is estimated at $\sim$55 μAh cm^{-2} μm^{-1} (where "cm^{-2}" and "μm^{-1}" refer to the geometric surface area and the whole thickness of the film, respectively), which corresponds to a discharge capacity of ca. 200 mAh g^{-1} (calculated from the Pd and Mg layer densities determined previously by RBS). Assuming, as a first approximation, that the inner and outer Pd layer were H-saturated (i.e. $PdH_{0.7}$) after charging, the H/Mg atomic ratio in the fully H-charged Pd/Mg/Pd film is estimated at $\sim$0.21, which is lower than the expected value for H-saturated Mg (H/Mg = 2). As stated in a previous study [13], this indicates that the formation of MgH_2 is confined at the Pd_{out}/Mg interface region (i.e. where the Mg–Pd interaction is maximal) and thus, a large part of the Mg layer does not participate in the electrochemical hydriding process.

For $x = 0.13$ (Fig. 5b), the discharge curves appear more discontinuous than for $x = 0$ with the presence of three short and not well-defined plateaus at ca. −0.8, −0.7 and −0.45 V, respectively. The discontinuities in the discharge curves reveal the presence of different types of H-occupation sites in the $Pd/Mg_{0.87}Al_{0.13}$/Pd film but the specific origin of these sites is presently unknown. Moreover, the discharge curve shape and duration do not change significantly with cycling, leading to a low H-discharge capacity ($\sim$36 μAh cm^{-2} μm^{-1} at the 10th cycle). Similar behaviour is observed for $x = 0.39$ (Fig. 5d) with the presence of a discontinuous discharge curve which evolves little with cycling, leading to a maximal discharge capacity of $\sim$48 μAh cm^{-2} μm^{-1} at the 10th cycle. The low hydrogen storage capacity of these films may be related to the absence of porosity in the $Mg_{1-x}Al_x$ layer for $x = 0.13$ and 0.39 (see RBS data), leading to a sharp Pd_{out}/Mg(Al) interface which is unfavourable for their hydriding as shown previously on dense Pd/Mg/Pd films [13]. In contrast, for $x = 0.21$ (Fig. 5c), major evolution in the discharge curve occurs upon cycling. After 10 cycles, the discharge curve displays an extended sloping plateau in the −0.9/−0.7 V potential region followed by a second shorter discharge plateau at ca. −0.4 V. The duration of the first plateau largely increases with cycling whereas the second one evolves much less during the successive charge/discharge cycles. On the basis of the discharge duration reached after 10 cycles (1400 s), the discharge capacity of the $Pd/Mg_{0.79}Al_{0.21}$/Pd film is estimated at $\sim$85 μAh cm^{-2} μm^{-1} or 320 mAh g^{-1}, which corresponds to a H/M atomic ratio of $\sim$0.48 (i.e. 1.9 wt% H) in the Mg–Al layer. This value is higher than the one obtained previously for $x = 0$ (H/M= 0.21 or 0.9 wt% H). It may be related to its higher porosity (28%) favouring the Pd_{out}/Mg(Al) interaction but also to the dissolution of Al in Mg phase that may induce the formation of an additional type of H-occupation site as illustrated by the presence of a second discharge step at −0.4 V (Fig. 5c). Note that the potential of this second discharge step is surprisingly high, reflecting its slow H-desorption kinetic and/or the high thermodynamic stability of the corresponding MH phase.

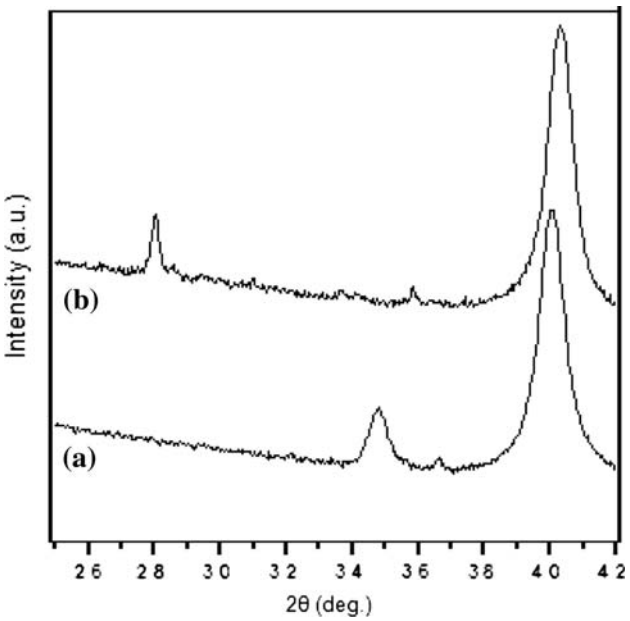

Fig. 6 XRD patterns of the $Pd/Mg_{0.79}Al_{0.21}$/Pd: (*a*) as-deposited, (*b*) after 5 charge/discharge cycles

In addition, as seen in Fig. 6, XRD analysis performed on cycled $Pd/Mg_{0.79}Al_{0.21}$/Pd film (5th cycle, discharge state) shows the disappearance of the Mg(Al) phase peaks, which may result from an amorphyzation of the Mg(Al) layer upon cycling. On the other hand, a new peak attributed to the MgH_2 phase is observed at 28.0°. Its presence in the discharged electrode state demonstrates that the hydrogen discharge reaction is partially irreversible in the present discharge conditions and thus, the H concentrations in the films determined previously form the discharge capacities must be underestimated. Further experiments (e.g. in situ XRD analyses upon cycling) are planned to clarify this issue.

Acknowledgements This work was financially supported by the Natural Sciences and Engineering Research Council (NSERC) of Canada. The authors thank Dr. Martin Chicoine (University of Montreal) for the RBS analyses.

References

1. Schlapbach L, Züttel A (2001) Nature 414:353
2. Wipf H (ed) (1997) Hydrogen in metals III: properties and applications, Topics in Applied Physics, vol 73. Springer-Verlag, Berlin

3. Oumellal Y, Rougier A, Nazri GA, Tarascon JM, Aymard L (2008) Nature Mater 7:916
4. Johansosson M, Ostenfeld CW, Chorkendorff I (2006) Phys Rev B 74:193408
5. Spatz P, Aebischer HA, Krozer A, Schlapbach L (1993) Z Phys Chem 181:393
6. Sakintuna B, Lamari-Darkrim F, Hirscher M (2007) Inter J Hydrogen Energy 32:1121
7. Huot J, Liang G, Schulz R (2001) Appl Phys A 72:187
8. Fujii H, Higuchi K, Yamamoto K, Kajioka H, Orimo S, Toiyama K (2002) Mater Trans 43:2721
9. Higuchi K, Kajioka H, Toiyama K, Fujii H, Orimo S, Kikuchi Y (1999) J Alloys Compd 293–295:484
10. Yoshimura K, Yamada Y, Okada M (2004) Surf Sci 566–568:751
11. Singh S, Eijt SWH, Zandbergen MW, Legerstee WJ, Svetchnikov VL (2007) J Alloys Compd 441:344
12. Checchetto R, Brusa RS, Bazzanella N, Karwasz GP, Spagolla M, Miotello A, Mengucci A, Di Cristoforo A (2004) Thin Solid Films 469–470:350
13. Bouhtiyya S, Roué L (2009) Inter J Hydrogen Energy 34:5778
14. Andreasen A (2008) Inter J Hydrogen Energy 33:7489
15. Domènech-Ferrer R, Sridharan MG, Garcia G, Pi F, Rodriguez-Viejo J (2007) J Power Sources 169:117
16. Garcia G, Domènech-Ferrer R, Pi F, Santiso J, Rodriguez-Viejo J (2007) J Comb Chem 9:230
17. Eason R (2006) Pulsed deposition of thin films: applications—led growth of functional materials. Wiley, NJ
18. Nayeb-Hashemi AA, Clarks JB (1988) Phase diagrams of binary magnesium alloys. ASM International, Metals Park, OH
19. Arnell RD, Bates RI (1992) Vacuum 43:105
20. Gremaud R, Borgschulte A, Chacon C, Van Mechelen JLM, Schreuders H, Zuttel A, Hjorvarsson B, Dam B, Griessen R (2006) Appl Phys A 84:77
21. Bouhtiyya S, Roué L (2008) Inter J Hydrogen Energy 33:2912